

Study of the reactions $e^+e^- \rightarrow \pi^+\pi^-\pi^0\pi^0\pi^0$ and $\pi^+\pi^-\pi^0\pi^0\eta$ at center-of-mass energies from threshold to 4.35 GeV using initial-state radiation by BaBar Collaboration - contents analysis

Kerim Guseynov

Based on arXiv:1810.1196

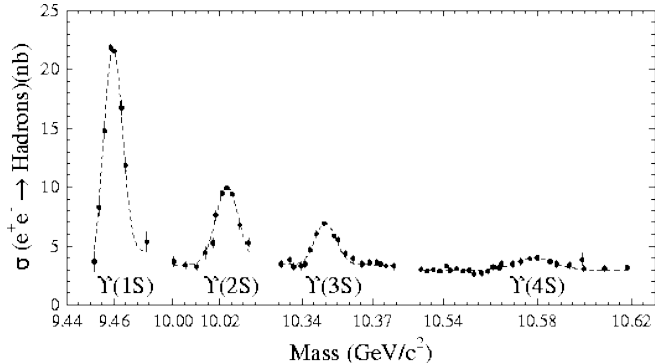
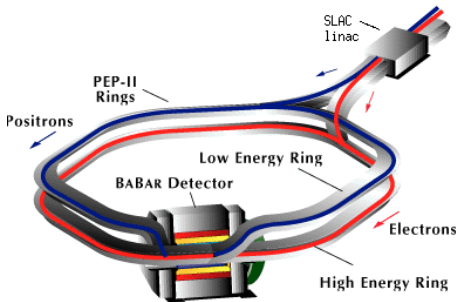
Faculty of Physics
Moscow State University

Nov 25, 2022

Introduction

- Initial-state radiation (ISR) includes events like $ee \rightarrow X\gamma$, where γ carries a huge momentum and comes from the initial ee before $ee \rightarrow X$.
- ISR gives access to a wide range of effective center-of-mass energies below the full ee c.m. energy.
- Gives access to low-energy cross-sections at high luminosity B -factories. Especially interesting for the muon $g - 2$ studies — the cross sections are required for the Standard Model calculations.
- In addition, IRS further facilitates resonance spectroscopy.

BaBar detector and data sample



$$\int d\mathcal{L} = 468.6 \text{ fb}^{-1}$$

Effective $E_{\text{c.m.}} < 4.35 \text{ GeV}$ to suppress $\Upsilon(4S)$ background.

- Vertex tracker

- Drift chamber

- Cherenkov detector

Monte Carlo simulation

- $ee \rightarrow \pi^+ \pi^- 3\pi^0 \gamma$
 - $\omega(782)\pi^0 \pi^0$
 $\omega(782) \rightarrow \pi^+ \pi^- \pi^0$
 $\pi^0 \pi^0$ produced both directly and via $f_0(980)$
 - $\eta\rho(770)$
 $\eta \rightarrow$ all measured modes
- $ee \rightarrow \pi^+ \pi^- 2\pi^0 \eta \gamma$
 - Phase-space model
 - $\omega\pi^0 \eta$
- Large background samples of both ISR and non-ISR processes.

Event selection

- Two pion tracks (from interaction region) and at least 7 photons.
- The largest-energy γ is considered the ISR one.
- The other 6 are grouped in two pairs around m_π and two independent ones: both π^0 and η .
- Each event is fit with signal hypothesis $ee \rightarrow \pi^+\pi^-3\pi^0\gamma$ and bkg hypothesis $ee \rightarrow \pi^+\pi^-2\pi^0\gamma$ (much larger cross-section).
 χ^2 from the fits are used later for bkg subtraction.

$\pi^+\pi^-3\pi^0$: event selection

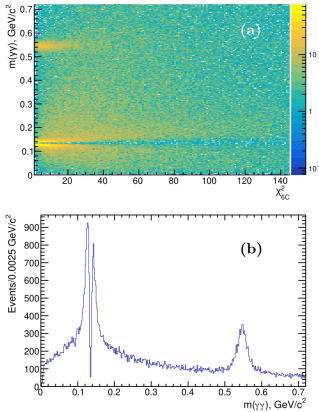


FIG. 1: (a) The invariant mass $m(\gamma\gamma)$ of the third photon pair vs $\chi^2_{2\pi 2\pi^0 \gamma\gamma}$. (b) The $m(\gamma\gamma)$ distribution for $\chi^2_{2\pi 2\pi^0 \gamma\gamma} < 60$ and with additional selection criteria applied as described in the text.

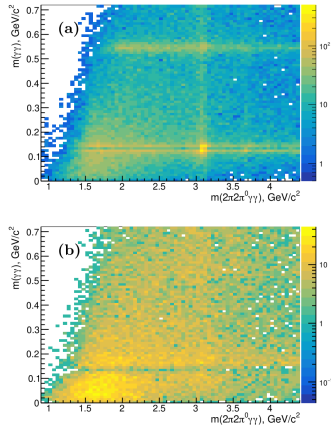


FIG. 2: (a) The third-photon-pair invariant mass $m(\gamma\gamma)$ vs $m(2\pi 2\pi^0 \gamma\gamma)$ for (a) $\chi^2_{2\pi 2\pi^0 \gamma\gamma} < 60$ and (b) $60 < \chi^2_{2\pi 2\pi^0 \gamma\gamma} < 120$.

$\pi^+\pi^-3\pi^0$: simulation

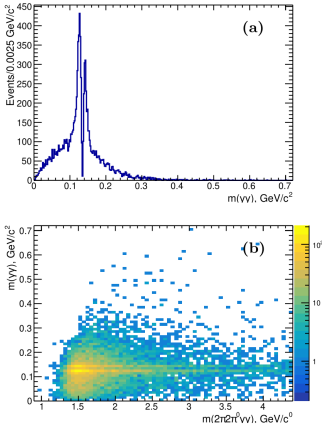


FIG. 3: The MC-simulated distribution for $e^+e^- \rightarrow \eta\pi^+\pi^-$ events of (a) the third-photon-pair invariant mass $m(\gamma\gamma)$, and (b) $m(\gamma\gamma)$ vs $m(\pi^+\pi^-2\pi^0\gamma\gamma)$.

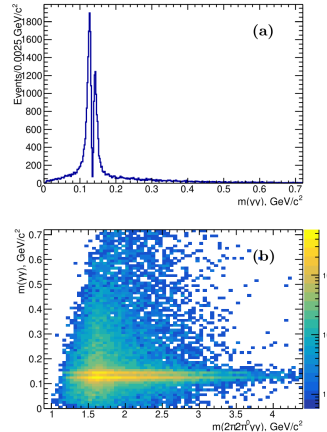


FIG. 4: The MC-simulated distribution for $e^+e^- \rightarrow \omega\pi^0\pi^0$ events of (a) the third-photon-pair invariant mass $m(\gamma\gamma)$, and (b) $m(\gamma\gamma)$ vs $m(\pi^+\pi^-2\pi^0\gamma\gamma)$.

$\pi^+\pi^-3\pi^0$: mass-dependent efficiency

For bins in $m(2\pi 2\pi^0 \gamma\gamma)$

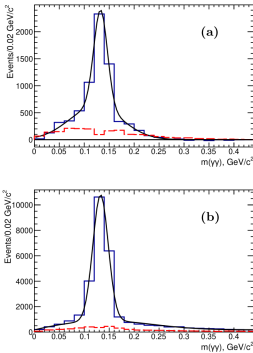


FIG. 5: The background subtracted MC-simulated $m(\gamma\gamma)$ distribution for (a) $e^+e^- \rightarrow \eta\pi^+\pi^-$ and (b) $e^+e^- \rightarrow \omega\pi^0\pi^0$ events. The dashed histogram shows the simulated distribution from the χ^2 control region, used for subtraction. The fit function is described in the text.

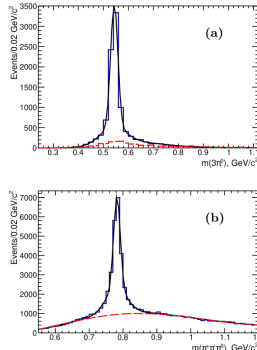


FIG. 6: (a) The background subtracted MC-simulated $3\pi^0$ invariant mass for the $e^+e^- \rightarrow \eta\pi^+\pi^-$ events. The dashed distribution is from the simulated χ^2 control region, used for background subtraction. (b) The $\pi^+\pi^-\pi^0$ invariant mass for the MC-simulated $e^+e^- \rightarrow \omega\pi^0\pi^0$ events (three entries per event). The solid curve shows the fit function used to obtain number of signal events. The dashed curve shows the fit function for the combinatorial background.

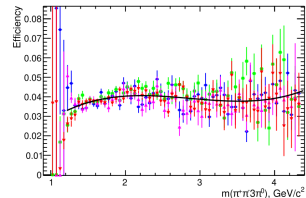


FIG. 7: The energy-dependent reconstruction efficiency for $e^+e^- \rightarrow \pi^+\pi^-\pi^0\pi^0$ events, determined using four different methods: see text. The curve shows the results of a fit to the average values, which is used in the cross section calculation.

$\pi^+\pi^-3\pi^0$: signal yields per $m(2\pi 2\pi^0 \gamma\gamma)$ bins

$14\,390 \pm 182$ in total

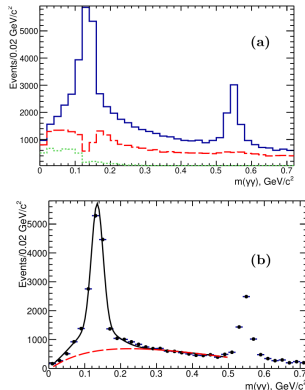


FIG. 8: (a) The third-photon-pair invariant mass $m(\gamma\gamma)$ for data in the signal (solid) and χ^2 control (dashed) regions. The dotted histogram shows the estimated background from $e^+e^- \rightarrow \pi^+\pi^-\pi^0\pi^0$. (b) The $m(\gamma\gamma)$ invariant mass for data after background subtraction. The curves are the fit results as described in the text.

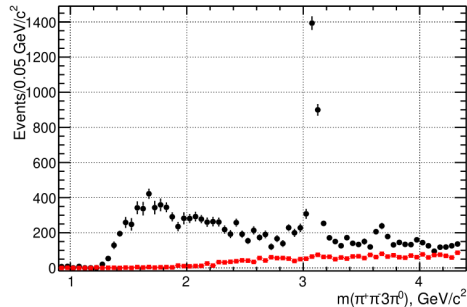


FIG. 9: The invariant mass distribution of $\pi^+\pi^-3\pi^0$ events, obtained from the fit to the π^0 mass peak. The contribution from non-ISR uds background is shown by squares.

$\pi^+\pi^-3\pi^0$: peaking background from non-ISR events

$ee \rightarrow \pi^+\pi^-3\pi^0\pi^0$ with $\pi^0 \rightarrow 2\gamma$, one γ very hard

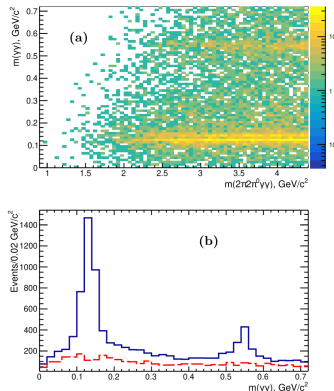


FIG. 10: (a) The third-photon-pair invariant mass vs $m(\pi^+\pi^-\pi^0\pi^0\gamma\gamma)$ for the uds simulation. (b) The projection plot for (a) the signal region $\chi^2_{2\pi2\pi^0\gamma\gamma} < 60$ (solid histogram), and the control region $60 < \chi^2_{2\pi2\pi^0\gamma\gamma} < 120$ (dashed histogram).

$$\sigma(2\pi3\pi^0)(E_{\text{c.m.}}) = \frac{dN_{5\pi\gamma}(E_{\text{c.m.}})}{d\mathcal{L}(E_{\text{c.m.}})\varepsilon_{5\pi}^{\text{corr}}\varepsilon_{5\pi}^{\text{MC}}(E_{\text{c.m.}})(1 + \delta_R)}$$

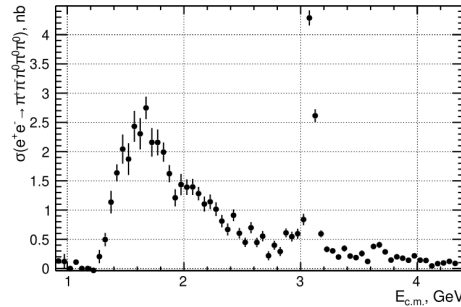


FIG. 11: The measured $e^+e^- \rightarrow \pi^+\pi^-\pi^0\pi^0\pi^0$ cross section. The uncertainties are statistical only.

$\pi^+\pi^-3\pi^0$: resonant structure: $\eta \rightarrow 3\pi^0$

$\eta \rightarrow 3\pi^0$ peak, $\pi^+\pi^-$ coming from $\rho(770)$

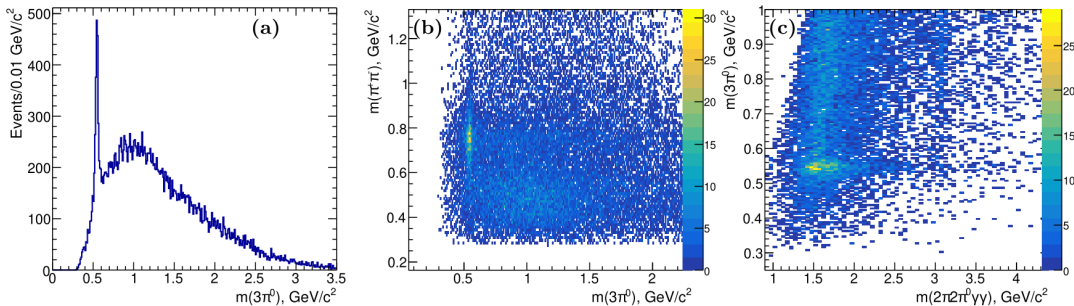


FIG. 12: (a) The $\pi^0\pi^0\pi^0$ invariant mass. (b) The $\pi^+\pi^-$ vs the $\pi^0\pi^0\pi^0$ invariant mass. (c) The $\pi^0\pi^0\pi^0$ invariant mass vs the five-pion invariant mass.

$\pi^+\pi^-3\pi^0$: resonant structure: $\eta \rightarrow 3\pi^0$

2102 ± 112 in total

ρ visible in η range, much less in sidebands

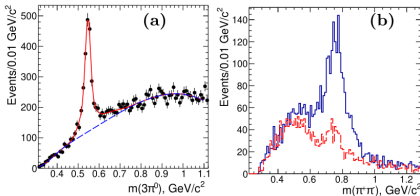


FIG. 15: (a) The $3\pi^0$ invariant mass for data. The curves show the fit functions. The solid curve shows the η peak (based on MC simulation) plus the non- η continuum background (dashed). (b) The $\pi^+\pi^-$ invariant mass for events selected in the η peak region. The dashed histogram shows the continuum events in the η -peak sidebands.

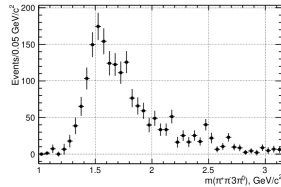


FIG. 16: The $m(\pi^+\pi^-3\pi^0)$ invariant mass dependence of the selected data events for $e^+e^- \rightarrow \eta\pi^+\pi^-, \eta \rightarrow 3\pi^0$.

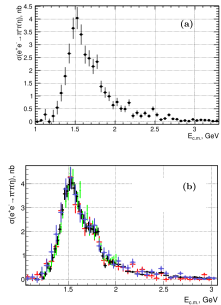


FIG. 17: (a) The energy dependent $e^+e^- \rightarrow \eta\pi^+\pi^-$ cross section obtained in the $2\pi 3\pi^0$ mode. (b) Comparison of the current results (squares) with previous measurements from BABAR in the $\eta \rightarrow \pi^+\pi^- \pi^0$ (upside-down triangles) [21] and $\eta \rightarrow \gamma\gamma$ modes (circles) [20]. Results from the SND experiment [22] are shown by triangles.

$\pi^+\pi^-3\pi^0$: resonant structure: $\omega \rightarrow \pi^+\pi^-\pi^0$

$\omega \rightarrow \pi^+\pi^-\pi^0$ peak, indications of $\phi, J/\psi$

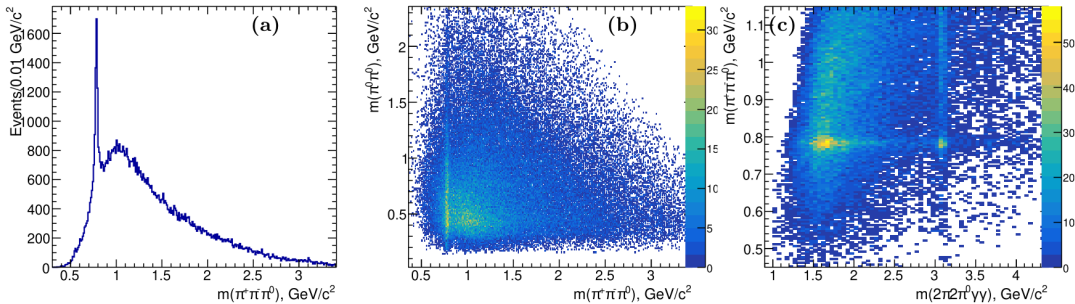


FIG. 13: (a) The $\pi^+\pi^-\pi^0$ invariant mass (three combinations per event). (b) The $\pi^0\pi^0$ vs the $\pi^+\pi^-\pi^0$ invariant mass. (c) The $\pi^+\pi^-\pi^0$ invariant mass vs the five-pion invariant mass.

$\pi^+\pi^-3\pi^0$: resonant structure: $\omega \rightarrow \pi^+\pi^-\pi^0$

3960 \pm 146 events in total, $f_0(980)$ not clearly visible in $m(\pi^0\pi^0)$, $\omega(1650)$ contribution
 Cross-section 2 times smaller than $e^+e^- \rightarrow \omega\pi^+\pi^-$, as expected from isospin symmetry

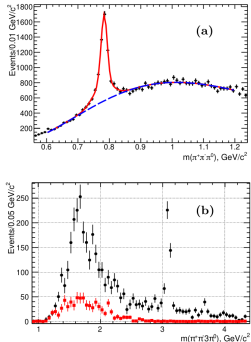


FIG. 18: (a) The $\pi^+\pi^-3\pi^0$ invariant mass for data. The solid curve shows the fit function for signal (based on MC-simulation) plus the combinatorial background (dashed curve). (b) The mass distribution of the $\pi^+\pi^-3\pi^0$ events in the ω peak (circles) and estimated contribution from the $\omega\pi^0$ background (squares).

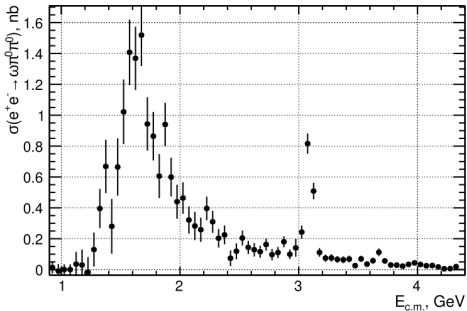


FIG. 19: The energy dependent $e^+e^- \rightarrow \omega\pi^0\pi^0$ cross section in the $\pi^+\pi^-3\pi^0$ mode.

$\pi^+\pi^-3\pi^0$: resonant structure: $\rho^\pm \rightarrow \pi^\pm\pi^0$

$\rho \rightarrow \pi\pi^0$ peak, intermediate $\rho^+\rho^-\pi^0$
 Clear J/ψ and indication of $\psi(2S)$

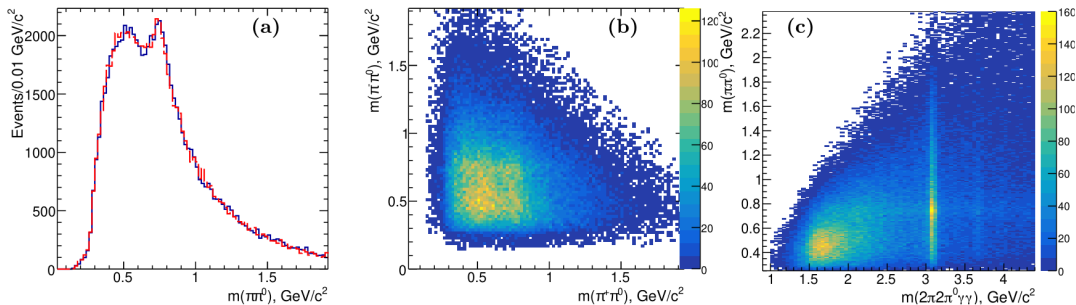


FIG. 14: (a) The $\pi^+\pi^0$ (solid) and $\pi^-\pi^0$ (dashed) invariant masses (three combinations per event). (b) The $\pi^-\pi^0$ vs the $\pi^+\pi^0$ invariant mass. (c) The $\pi^\pm\pi^0$ invariant mass vs the five-pion invariant mass.

$\pi^+\pi^-3\pi^0$: resonant structure: $\rho^\pm \rightarrow \pi^\pm\pi^0$

$14\,894 \pm 501$ events in total,

correlated $\rho^+\rho^-\pi^0$ production decreases with $m(5\pi)$

Statistics not significant for ρ decays resonant sub-sub-structure

Sum of intermediate states does give the full cross-section

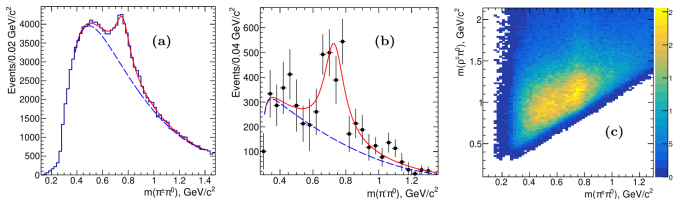


FIG. 20: (a) The $\pi^\pm\pi^0$ invariant mass for data. The dashed curve shows the fit to the combinatorial background. The solid curve is the sum of the background curve and the BW function for the ρ^\pm . (b) The result of the ρ^+ fit in bins of $0.04 \text{ GeV}/c^2$ in the ρ^- mass. (c) Scatter plot of the $\rho^\pm\pi^0$ invariant mass vs the $\pi^\mp\pi^0$ invariant mass.

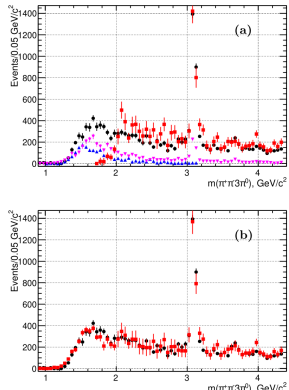


FIG. 21: (a) Number of events in bins of $E_{\text{c.m.}}$ from the $\eta\pi^+\pi^-$ (triangles), $\omega\pi^0\pi^0$ (upside-down triangles), and $\rho\rightarrow\pi\pi^0$ (squares) intermediate states. The circles show the total event numbers obtained from the fit to the π^0 peak. (b) The circles as are described for (a). The squares show the sums of event numbers with η , ω and the ρ contribution for correlated $\rho^+\rho^-$ production.

$\pi^+\pi^-2\pi^0\eta$: signal yields per $m(2\pi2\pi^0\gamma\gamma)$ bins

4700 ± 84 events in total

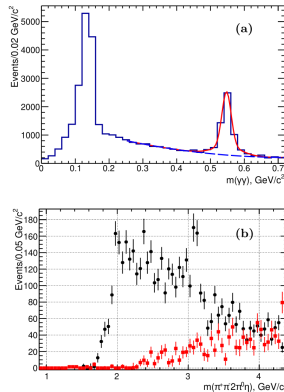


FIG. 22: (a) The third-photon-pair invariant mass for data. The dashed curve shows the fitted background. The solid curve shows the sum of background and the two-Gaussian fit function used to obtain the number of events with an η . (b) The invariant mass distribution for the $\pi^+\pi^-2\pi^0\eta$ events obtained from the η signal fit. The contribution of the uds background events is shown by the squares.

$\pi^+\pi^-2\pi^0\eta$: mass-dependent efficiency

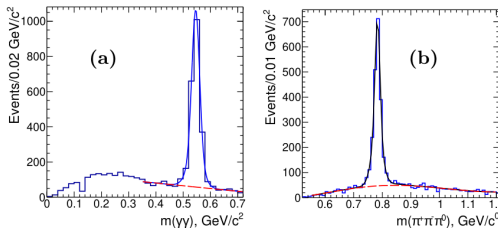


FIG. 23: (a) The third-photon-pair invariant mass for simulation of the $e^+e^- \rightarrow \pi^+\pi^-\pi^0\pi^0\eta\gamma$ process. The dashed curve shows the fitted background. The solid curve shows the sum of background and the two-Gaussian fit function used to obtain the number of events with an η . (b) The $\pi^+\pi^-\pi^0$ invariant mass for simulation. The solid curve shows a two-Gaussian fit function for the ω signal plus the combinatorial background (dashed).

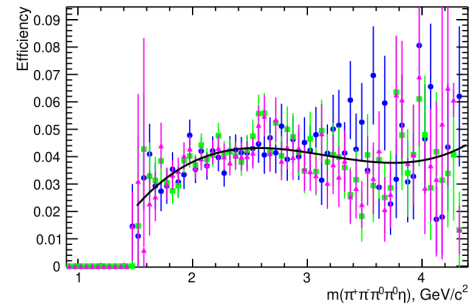


FIG. 24: The energy dependent detection efficiency, determined in three different ways: see text. The curve shows the fit to the average of the three and is used in the cross section determination.

$\pi^+\pi^-2\pi^0\eta$: cross-section

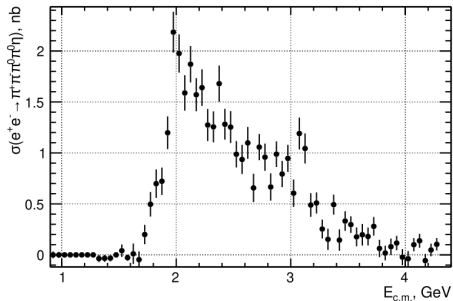


FIG. 25: Energy dependent cross section for $e^+e^- \rightarrow \pi^+\pi^-\pi^0\pi^0\eta$. The uncertainties are statistical only.

$\pi^+\pi^-2\pi^0\eta$: resonant structure: tiny $\eta(1285) \rightarrow \pi^0\pi^0\eta$

$\eta(1285)$ small but clear compared to sideband (red). No major structures

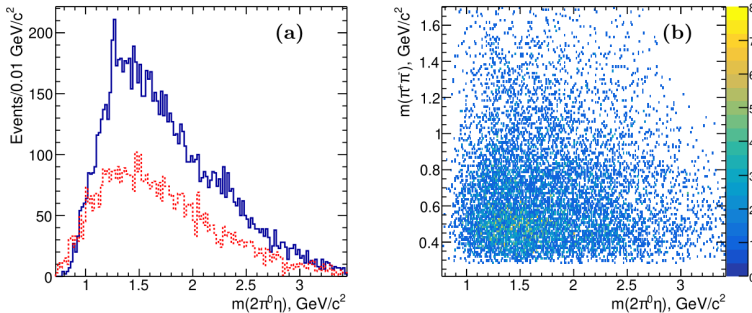


FIG. 26: (a) The $2\pi^0\eta$ invariant mass of the selected $\pi^+\pi^-2\pi^0\eta$ events (solid histogram), and the background determined from the χ^2 sideband (dotted histogram). (b) The $\pi^+\pi^-$ vs the $2\pi^0\eta$ mass for the selected events.

$\pi^+\pi^-2\pi^0\eta$: resonant structure: $\omega \rightarrow \pi^+\pi^-\pi^0$

$\omega \rightarrow \pi^+\pi^-\pi^0$ huge peak, ϕ at 1 GeV
 $a_0(980) \rightarrow \eta\pi^0$ correlation with ω

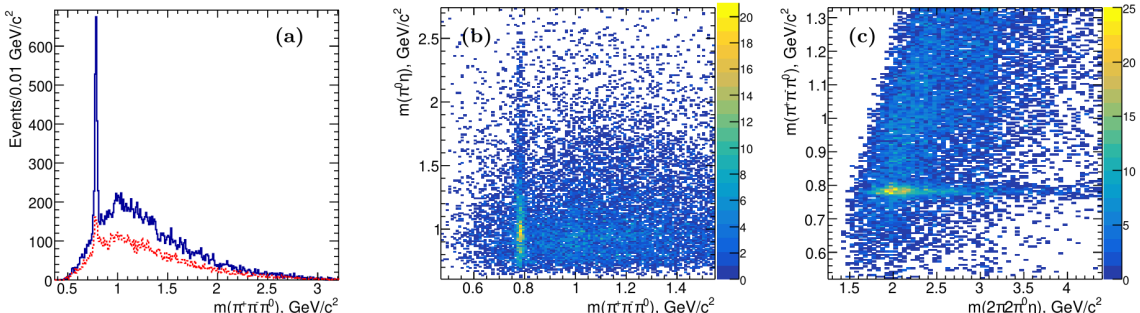


FIG. 27: (a) The $\pi^+\pi^-\pi^0$ invariant mass with two entries per event (solid histogram) and the background estimate from the η sideband (dotted histogram). (b) The $\pi^0\eta$ vs the $\pi^+\pi^-\pi^0$ invariant mass. (c) The $\pi^+\pi^-\pi^0$ invariant mass vs the $\pi^+\pi^-2\pi^0\eta$ invariant mass.

$\pi^+\pi^-2\pi^0\eta$: resonant structure: $\omega \rightarrow \pi^+\pi^-\pi^0$

1676 ± 22 events for ω and 269 ± 68 events for ϕ
 Clear $a_0(980)$ in ω peak but not its sidebands

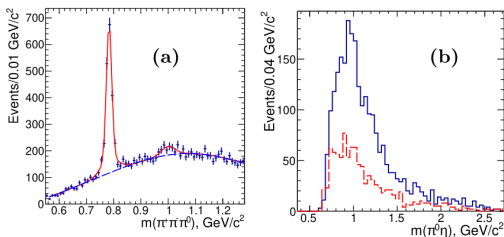


FIG. 29: (a) The $\pi^+\pi^-\pi^0$ invariant mass for data. The dashed curve describes the non-resonant background. The solid curve shows the sum of the background and the fit functions for the ω and ϕ contributions, described in the text. (b) The $\pi^0\eta$ invariant mass distribution for the events selected in the ω peak (solid). The dashed histogram shows the distribution from the ω -peak side band.

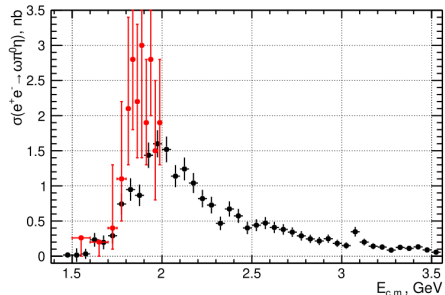


FIG. 30: The $E_{\text{c.m.}}$ dependence of the $e^+e^- \rightarrow \omega\pi^0\eta$ cross section (circles) in comparison with the SND results [31] (squares).

$\pi^+\pi^-2\pi^0\eta$: resonant structure: $\rho^\pm \rightarrow \pi^\pm\pi^0$

$\rho \rightarrow \pi\pi^0$ peaks, $\rho^+\rho^-$ correlation again

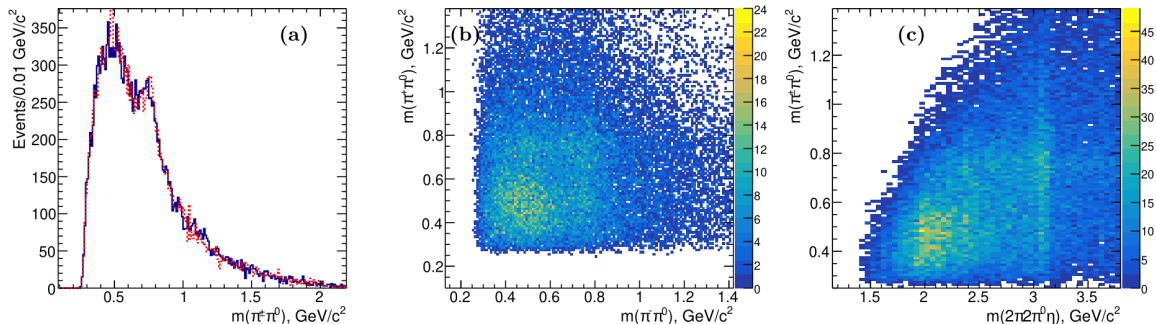


FIG. 28: (a) the $\pi^+\pi^0$ (solid) and $\pi^-\pi^0$ (dotted) invariant mass for the selected $\pi^+\pi^-2\pi^0\eta$ events (two entries per event). (b) The $\pi^-\pi^0$ vs the $\pi^+\pi^0$ invariant mass for the selected events. (c) The $\pi^\pm\pi^0$ invariant mass vs the $\pi^+\pi^-2\pi^0\eta$ invariant mass.

$\pi^+\pi^-2\pi^0\eta$: resonant structure: $\rho^\pm \rightarrow \pi^\pm\pi^0$

2908 ± 202 events, intermediate $a_0(980)\rho\pi$ is present

Sum of intermediate states is equal to the full cross-section except in the region around 2 GeV

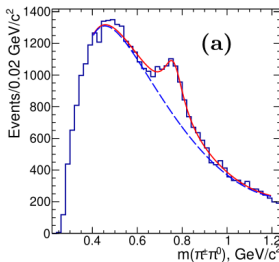


FIG. 31: (a) The $\pi^\pm\pi^0$ invariant mass for data. The curves show the fit functions, described in the text. (b) The $\pi^\pm\eta$ vs the $\pi^\mp\pi^0$ invariant mass.

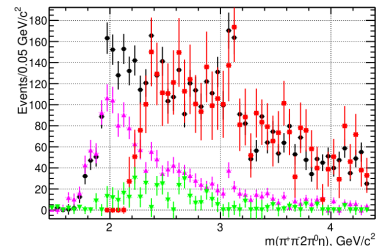
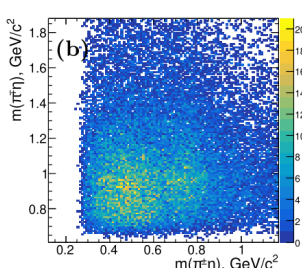


FIG. 32: Number of events in bins of $E_{c.m.}$ for inclusive $\pi^+\pi^-2\pi^0\eta$ events (circles) and for the $\omega\pi^0\eta$ (triangles), $\phi\pi^0\eta$ (upside-down triangles), and $\rho^\pm\pi^\mp\pi^0\eta$ (squares) intermediate states.

J/ψ region in $m(\pi^+\pi^-3\pi^0)$

2389 ± 63 events with J/ψ and 177 ± 27 with $\psi(2S)$
 including 142 ± 21 events of $\psi(2S) \rightarrow J/\psi\pi^0\pi^0 \rightarrow 5\pi$

$$B_{J/\psi \rightarrow 5\pi} = (2.70 \pm 0.07 \pm 0.27) \times 10^{-2}$$

$$B_{\psi(2S) \rightarrow 5\pi} = (5.2 \pm 0.8 \pm 0.5) \times 10^{-3}$$

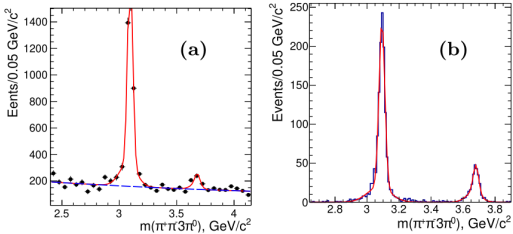


FIG. 33: (a) The $\pi^+\pi^-3\pi^0$ mass distribution for ISR-produced $e^+e^- \rightarrow \pi^+\pi^-\pi^0\pi^0\pi^0$ events in the $J/\psi-\psi(2S)$ region. (b) The MC-simulated signals. The curves show the fit functions described in the text.

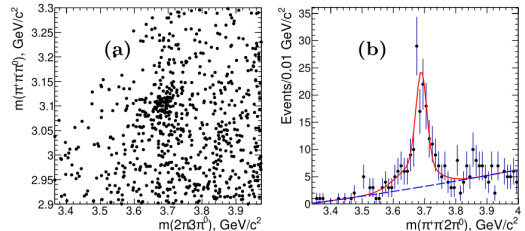


FIG. 34: (a) The three-pion combination closest to the J/ψ mass vs the five-pion mass. (b) The five-pion mass for the events with the three-pion mass in the ± 50 MeV/c^2 interval around the J/ψ mass. The curves show the fit functions for all events (solid) and the contribution of the background (dashed).

J/ψ region in $m(\pi^+\pi^-3\pi^0)$: intermediate 5π states

$$B_{J/\psi \rightarrow \omega\pi^0\pi^0} = (5.04 \pm 0.37 \pm 0.50) \times 10^{-3} \quad B_{\psi(2S) \rightarrow \omega\pi^0\pi^0} = (1.1 \pm 0.3 \pm 0.1) \times 10^{-3}$$

$B_{J/\psi \rightarrow \omega\pi^0\pi^0}$ lower than for $\omega\pi^+\pi^-$ by a factor of two, as expected from isospin symmetry, again

$$B_{J/\psi \rightarrow \rho^\pm\pi^\mp\pi^0\pi^0} = (1.40 \pm 0.12 \pm 0.14 \pm 0.10) \times 10^{-2} \quad B_{J/\psi \rightarrow \rho^+\rho^-\pi^0} = (0.60 \pm 0.05 \pm 0.06 \pm 0.05) \times 10^{-2}$$

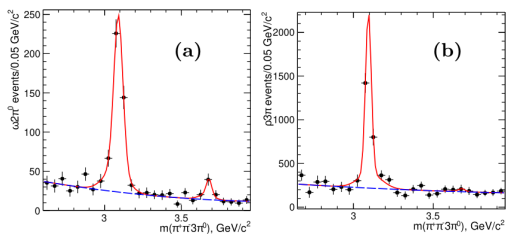


FIG. 35: (a) The five-pion mass for events with the three-pion combination in the $\omega(782)$ mass region. (b) The five-pion mass for events with $\pi^\pm\pi^0$ combination in the $\rho(770)$ mass region. The curves show the fit functions described in the text.

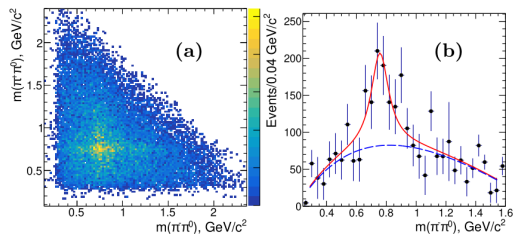


FIG. 36: (a) Scatter plot of the $\pi^+\pi^0$ vs the $\pi^-\pi^0$ invariant mass for the J/ψ region in Fig. 35(b). (b) Number of $\pi^+\pi^0$ events in bins of 0.04 GeV/c^2 in the $\pi^-\pi^0$ mass. The curves show the fit functions for all events (solid) and the contribution of the background (dashed).

J/ψ region in $m(\pi^+\pi^-2\pi^0\eta)$

203 ± 29 $J/\psi \rightarrow \pi^+\pi^-2\pi^0\eta$ decays, 27 ± 14 $J/\psi \rightarrow \omega\pi^0\eta$ decays, 168 ± 62 $J/\psi \rightarrow \rho^\pm\pi^\mp\pi^0\pi^0$ decays

$$B_{J/\psi \rightarrow \pi^+\pi^-\pi^0\pi^0\eta} = (2.30 \pm 0.33 \pm 0.35) \times 10^{-3} \quad B_{J/\psi \rightarrow \omega\pi^0\eta} = (3.4 \pm 1.6 \pm 0.6) \times 10^{-4}$$

$$B_{J/\psi \rightarrow \rho^\pm\pi^\mp\pi^0\eta} = (1.9 \pm 0.7 \pm 0.3) \times 10^{-3} \quad B_{\psi(2S) \rightarrow \pi^+\pi^-\pi^0\pi^0\eta} < 3.5 \times 10^{-4} \text{ at 90% C.L.}$$

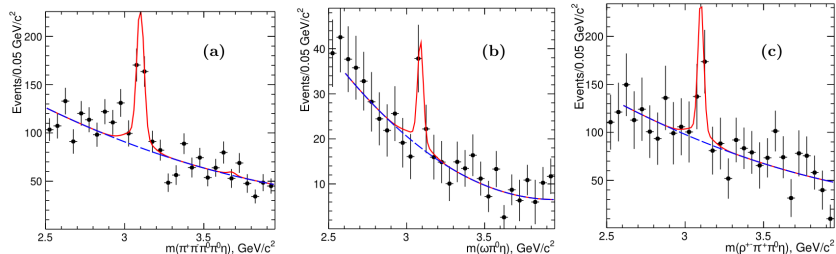


FIG. 37: The J/ψ region for the (a) $\pi^+\pi^-2\pi^0\eta$, (b) $\omega\pi^0\eta$, and (c) $\rho^\pm\pi^\mp\pi^0\eta$ events. The curves show the fit functions described in the text.

Summary

- Two ee annihilation processes with 5 final state particles were studied at a range center-of-mass energies.
- Their cross-sections measured as functions of c.m. energy.
- Resonant structure comprehensively investigated including sub-process cross-section measurements.
- Branching fractions of several J/ψ and $\psi(2S)$ decay modes measured for the first time.